Multipolar ordering from dynamical mean field theory with application to CeB$_6$

Junya Otsuki [ID],[1] Kazuyoshi Yoshimi [ID],[2] Hiroshi Shinaoka,[3] and Harald O. Jeschke [ID][1]

[1]*Research Institute for Interdisciplinary Science, Okayama University, Okayama 700-8530, Japan*
[2]*Institute for Solid State Physics, University of Tokyo, Chiba 277-8581, Japan*
[3]*Department of Physics, Saitama University, Saitama 338-8570, Japan*

Magnetic and multipolar ordering in f electron systems takes place at low temperatures of order 1–10 Kelvin. Combinations of first-principles with many-body calculations for such low-energy properties of correlated materials are challenging problems. We address multipolar ordering in f electron systems based on the dynamical mean-field theory (DMFT) combined with density functional theory. We derive the momentum-dependent multipolar susceptibilities and interactions in two ways: by solving the Bethe-Salpeter (BS) equation of the two-particle Green's function and by using a recently developed approximate strong-coupling formula. We apply the formalism to the prototypical example of multipolar ordering in CeB$_6$ using the Hubbard-I solver, and demonstrate that the experimental quadrupole transition is correctly reproduced. The results by the approximate formula show good agreement with those by the BS equation. This first-principles formalism for multipolar ordering based on DMFT has applications which are beyond the reach of the traditional RKKY formula. In particular, more itinerant electron systems including $5f$, $4d$, and $5d$ electrons can be addressed.

I. INTRODUCTION

Recent progress in electronic structure calculations has been expanding the target of first-principles calculations to strongly correlated materials, in particular with the help of the DMFT [1–3]. The DMFT combined with density functional theory (DFT+DMFT) has been employed extensively to investigate the electronic structure of transition-metal oxides [4–7], of iron-based superconductors [8–10], of rare-earth compounds [11,12], and of many other materials where electronic correlations in the form of local Coulomb repulsion or Hund's rule coupling are crucial. DFT+DMFT is often employed for the theoretical support of photoemission experiments [13]. There is an ongoing effort to account for the momentum dependence of the self-energy [14], and the efficacy of new approaches is often demonstrated for the prime example of a moderately correlated oxide, SrVO$_3$. For example, DMFT has been combined with the *GW* method [15,16], with vertex corrections [17,18] or improved by the dynamical cluster approximation [19].

The description of phase transitions in correlated materials is one of the objectives in DFT+DMFT investigations [20]. Typical examples include metallic ferromagnetism in elemental Fe [21–27], isostructural transitions in elemental Ce [28–32], the orbital ordering in Cu fluorides [33,34]. The intersite interactions between localized moments including multipolar degrees of freedom were formulated [35,36]. Ordered magnetism has been studied within DFT+DMFT [37–41], but such investigations are less routine than the application to paramagnetic phases. In particular, the determination of two-particle susceptibilities for comparison with inelastic neutron scattering continues to be difficult [42–45].

In this direction, multipolar ordering in rare-earth compounds is a challenging subject because of the f orbital degrees of freedom, the strong spin-orbit coupling, and the small energy scale of order 10 K or even less. In this paper, we address multipolar ordering based on the DFT+DMFT method. Conventionally, the multipolar ordering is considered by RKKY interactions where f electrons are treated as localized. On the other hand, a nonmagnetic Fermi liquid (heavy-fermion) ground state can be addressed from the opposite limit with itinerant f electrons. Actually, the localized and itinerant f states are continuously connected in a T-P phase diagram (Fig. 1). DMFT provides descriptions of the crossover between localized state and itinerant state including the heavy-fermion state near the quantum critical point [46–48]. Therefore, a formalism based on DMFT covers the whole region of the phase diagram. This motivates us to establish descriptions of multipolar ordering based on the DFT+DMFT framework for future wider applications such as mixed-valent rare-earth compounds and actinide compounds with itinerant $5f$ electrons.

We focus on CeB$_6$ as a prototypical material for multipolar ordering (for a review, see Ref. [49]). The $4f^1$ configuration in trivalent Ce ions forms a Γ_8 quartet ground state with total angular momentum $j = 5/2$ under the cubic crystalline electric field (CEF) [50]. Due to the fourfold degeneracy of the CEF multiplet, CeB$_6$ shows a rich phase diagram as shown in Fig. 2. Two phase transitions have been observed at low temperatures [51]. Below $T_Q = 3.4$ K, CeB$_6$ exhibits the antiferroquadrupole (AFQ) order with $\boldsymbol{q} = (1/2, 1/2, 1/2)$ (phase II) [52–54]. The order parameter is the (xy, yz, zx)-type quadrupole, but the zero-field state is still under debate [55]. At $T_N = 2.3$ K, the antiferromagnetic (AFM) order takes place on top of the AFQ order (phase III) [56]. Furthermore, another phase appears when Ce is partially substituted with La (phase IV) [57]. This phase was ascribed to the antiferro-octupole order [58–60].
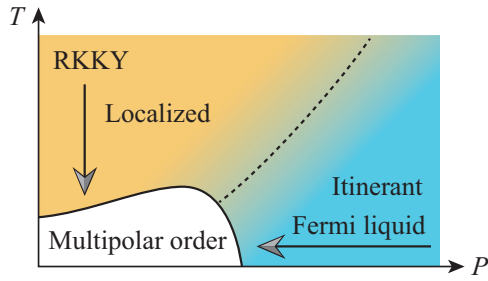
FIG. 1. A schematic P-T phase diagram of f electron materials and two contrasting approaches to the multipolar ordering.

Theoretically, the phase transitions in CeB_6 are described by 15 multipoles in the Γ_8 quartet states [62]. Since the $4f$ electrons are well localized in CeB_6 [63], a model consisting only of the local degrees of freedom is a good starting point. Based on a Heisenberg-type model for multipoles, Shiina *et al.* derived the T-H phase diagram and observables related to the order parameter [64,65]. In this approach, the coupling constants are determined so that the model yields results consistent with experiments.

Another important issue beyond phenomenology is the microscopic derivation of the multipolar interactions to understand why the multipolar ordering takes place in individual materials. Shiba *et al.* analyzed the RKKY formula in the Γ_8 systems and deduced general properties [66]. Evaluation of the multipolar interactions was performed later taking explicit electronic structures into account for CeB_6 [67–70], NpO_2 [71], and Pr compounds [72].

In the following, we present an application of the DFT+DMFT method to CeB_6 and reproduce the experimental order parameter. In Sec. II, we first present the single-particle excitation spectrum, and establish how to fix parameters such as the Coulomb repulsion U so that the method is applicable to other materials without any tuning parameter. In Sec. III, the momentum-dependent multipolar susceptibilities and interactions are derived in two ways: the one using the Bethe-Salpeter equation and a recently developed approximate formula based on the decoupling of the two-particle Green's function [73]. It will be demonstrated that the approximate formula can be used instead of the BS equation and shows good agreement with the experiments.
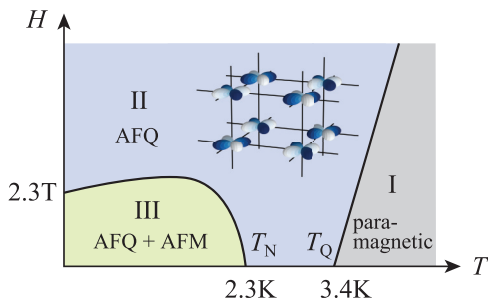

FIG. 2. A schematic T-H phase diagram of CeB_6 ($H \parallel [0, 0, 1]$) [57,61]. The lattice shows the configuration of the AFQ order in phase II, where the color indicates the sign of the xy-type quadrupole.
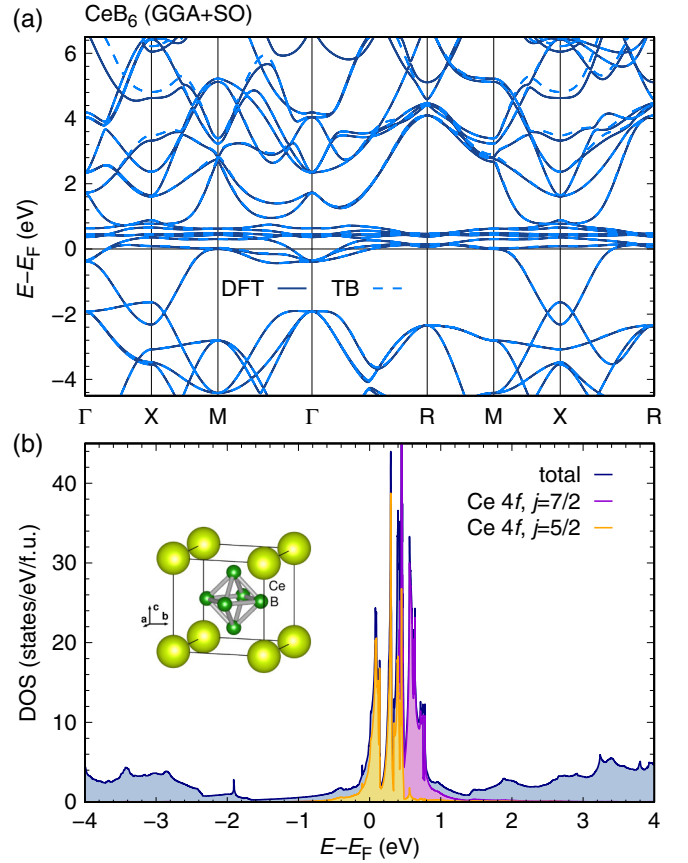

FIG. 3. (a) Fully relativistic band structure of CeB_6 (full lines), shown together with the tight binding bands obtained from projective Wannier functions (dashed lines). High symmetry points of the cubic $Pm\bar{3}m$ space group are $\Gamma = (0, 0, 0)$, $R = (1/2, 1/2, 1/2)$, $M = (1/2, 1/2, 0)$, $X = (1/2, 0, 0)$. (b) Total and orbital-resolved density of states. The $Pm\bar{3}m$ crystal structure of CeB_6 is shown as inset.

II. SINGLE-PARTICLE PROPERTIES

A. DFT calculations

The starting point of our study is a precise DFT calculation for CeB_6. We determine its fully relativistic electronic structure using the full potential local orbital (FPLO) basis set [74]. The calculations are performed based on a single-crystal x-ray diffraction structure determined at $T = 165$ K [75]. It has a cubic space group $Pm\bar{3}m$ and features one Ce atom in the corner of the cubic cell and a B_6 octahedron in its center as shown in the inset of Fig. 3(b). The DFT bands are shown in Fig. 3(a) (full lines). We use symmetry-protected maximally projected Wannier functions [76,77] to construct a 72-band model consisting of Ce $4f$ and $5d$ as well as B $2s$ and $2p$ orbitals; the resulting tight binding representation of the bands is shown as dashed lines in Fig. 3(a). Figure 3(b) shows the density of states (DOS). The Ce $4f$ partial DOS is resolved by the total angular momentum j contributions. The energy splitting Δ_{SOC} between $j = 5/2$ and $j = 7/2$ due to the spin-orbit coupling (SOC) is $\Delta_{SOC} = 0.32-0.34$ eV, which is comparable to the value in the Ce ion. The CEF splitting between the Γ_8 quartet ground state and the excited

TABLE I. Summary of the energy separation between occupied $4f^1$ state and Fermi level Δ_- and between occupied $4f^1$ state and lowest lying $4f^2$ state Δ_+ in units of eV.

Material	Δ_-	Δ_+
CeB$_6$ (experiment)	1.9 [81–83]	–
Ce (experiment)	0.27–1.92 [84]	3.46 [84]
Ce (theory)	1.9 [85]	3.1 [86]

Γ_7 doublet is 11.3 meV ($\approx$131 K), which is smaller by a factor of 4 compared to the experimental value 540 K [50].

B. DMFT calculations

Within the DFT+DMFT method, the single-particle Green's function matrix $\hat{G}(\boldsymbol{k}, i\omega_n)$ is given by [2]

$$\hat{G}(\boldsymbol{k}, i\omega_n) = [(i\omega_n + \mu)\hat{I} - \hat{H}_{\text{DFT}}(\boldsymbol{k}) - \hat{\Sigma}_{\text{loc}}(i\omega_n) + \hat{\Sigma}_{\text{DC}}]^{-1}, \tag{1}$$

where quantities with hat stand for 72×72 matrices. ω_n is the fermionic Matsubara frequency, μ is the chemical potential, and $\hat{I}$ is the identity matrix. $\hat{H}_{\text{DFT}}(\boldsymbol{k})$ denotes the noninteracting tight-binding Hamiltonian constructed by the DFT calculations. $\hat{\Sigma}_{\text{loc}}(i\omega_n)$ is the local self-energy in DMFT, and $\hat{\Sigma}_{\text{DC}}$ is the double-counting (DC) correction.

The local self-energy $\hat{\Sigma}_{\text{loc}}(i\omega_n)$ is computed by solving the effective impurity problem for f orbitals. We treat only $j = 5/2$ states, neglecting $j = 7/2$ states (j-j coupling scheme). The influence of the neglected $j = 7/2$ multiplet was analyzed in detail in Refs. [78,79]. We employ fully rotationally invariant Slater interactions, which are specified by four parameters called Slater integrals F_0, F_2, F_4, and F_6. We use the standard parametrization that relates the Slater integrals to two intuitive parameters, the Coulomb repulsion U and the Hund's coupling J_H [80].

We represent the DC self-energy in a simple form

$$\hat{\Sigma}_{\text{DC}} = -\Delta\epsilon_f \hat{N}_f, \tag{2}$$

where $\hat{N}_f$ is a projection onto f orbitals. $\Delta\epsilon_f$ stands for the energy shift of the single-particle energy of the f electrons. This expression is motivated by the fact that the local electronic structure such as the SOC and the CEF are already taken into account by the DFT and do not need to be changed. The $\hat{\Sigma}_{\text{DC}}$ cancels only the averaged Hartree shift in $\hat{\Sigma}_{\text{loc}}(i\omega_n)$ so that $4f$ electrons remain on the Ce atom.

We thus need to determine the three parameters U, J_H, and $\Delta\epsilon_f$, and we now explain how we arrive at $U = 6.2$ eV, $J_H = 0.8$ eV, and $\Delta\epsilon_f = -1.6$ eV. We do this based on the demand that the calculated single-particle excitation spectrum should agree with the experimental and theoretical photoemission spectroscopy (PES) and bremsstrahlung isochromat spectroscopy (BIS) spectra (for BIS, we resort to elemental Ce). Two energies characterize the spectrum: Δ_- is the minimum excitation energy from the occupied $4f^n$ multiplet to the Fermi energy E_F, and Δ_+ is the minimum excitation energy from E_F to empty $4f^{n+1}$ multiplets. Table I summarizes Δ_- and Δ_+ in the literature. From the PES experiment in CeB$_6$, Δ_- has been reported to be $\Delta_- = 1.9$ eV. On the other hand, the BIS spectrum is not available for CeB$_6$, and
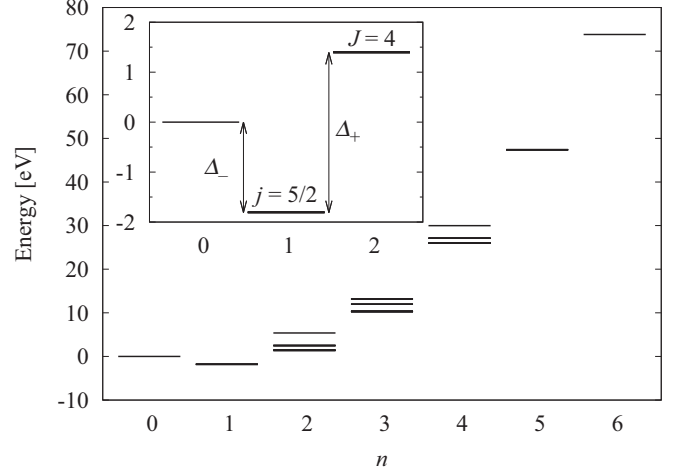

FIG. 4. Eigenenergies of the many-body states of local $4f$ electrons. The inset shows a zoom up of the low-energy multiplets.

we use the data for elemental Ce instead. The experiment reported $\Delta_+ = 3.46$ eV, while theoretical calculation yields $\Delta_+ = 3.1$ eV. We adopt the theoretical value, since the theoretical result for Δ_- in Ce agrees with the PES value for CeB$_6$. From these observations, we adopt $\Delta_- = 1.9$ eV and $\Delta_+ = 3.1$ eV. In Appendix A, we show how this leads to $U = 6.2$ eV, $J_H = 0.8$ eV, and $\Delta\epsilon_f = -1.6$ eV.

The DFT+DMFT calculations were performed using open source software DCORE [87] implemented on TRIQS [88] and DFTTOOLS [89] libraries. We solved the effective impurity model by exact diagonalization using POMEROL [90]. Here, we neglected the effective hybridization $\Delta(i\omega_n)$. This corresponds to the Hubbard-I approximation, which is often used for descriptions of properties of rare-earth compounds [91–94]. In fact, the Hubbard-I solver is a suitable choice for the present purpose of descriptions of the multipolar susceptibilities, in which the preservation of symmetry is relevant: We need at least three bath sites (six states including spins) to represent the hybridization of the $j = 5/2$ orbitals, which makes it difficult to compute the two-particle Green's function for the BS equation. The de facto standard solver for DMFT, namely, the continuous-time quantum Monte Carlo method [95] approximates the interaction to density-density type to avoid a negative sign problem, which again breaks the symmetry of multipoles. Note that an approximate treatment of rotationally invariant Slater interactions was shown to improve the ferromagnetic transition temperature of elemental iron [25]. Furthermore, in CeB$_6$, the Fermi surface is quite similar to that of LaB$_6$ [63,83], indicating that the $4f$ electrons are well localized. The Kondo temperature was estimated to be of the order of 1 K in experiments [96,97]. Therefore, a reasonable description is expected by the Hubbard-I approximation, which yields the correct Néel temperature for $U/W \gtrsim 1$ (W is the band width) as demonstrated in Ref. [73].

Without $\Delta(i\omega_n)$, energy levels of the many-body $4f$ states are well defined. Figure 4 shows the eigenvalues of the $4f^n$ multiplets for $U = 6.2$ eV, $J_H = 0.8$ eV, and $\Delta\epsilon_f = -1.6$ eV. The corresponding Slater integrals are $F_0 = 6.2$ eV, $F_2 = 9.54$ eV, $F_4 = 6.37$ eV, and $F_6 = 4.71$ eV. There are $2^6 = 64$
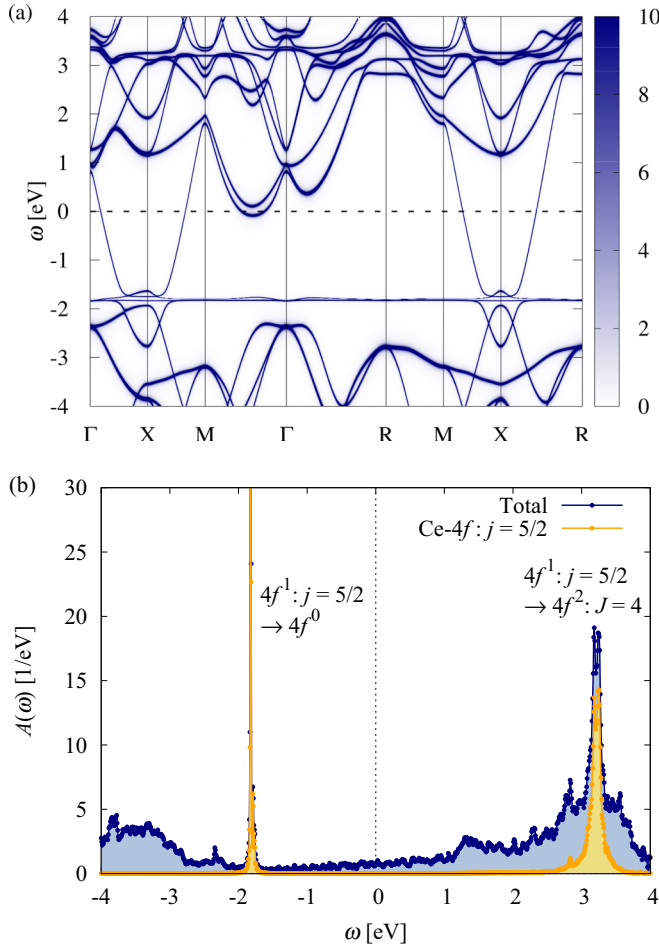
(a)

(b)

FIG. 5. (a) The single-particle excitation spectrum $A(\boldsymbol{k}, \omega)$ computed within DMFT. Only $j = 5/2$ states are retained. A broadening of width $\delta = 0.01$ eV is introduced. (b) The $\boldsymbol{k}$-integrated spectrum $A(\omega)$ at a temperature $T = 0.01$ eV. The labels near the peaks indicate the initial and final states in the excitation process.

levels in this figure. The CEF splitting is not visible on this scale, and we discuss only the multiplets labeled by the total angular momentum J. The energy of the $j = 5/2$ multiplet of the $4f^1$ configuration is $E_1 = -1.9$ eV ($\Delta_- = -E_1$). The $4f^2$ configuration has three multiplets, $J = 4, 2, 0$. The Hund's ground state $J = 4$ is located at $E_2 = +1.2$ eV, thus $\Delta_+ = E_2 - E_1 = 3.1$ eV.

The final results for the single-particle excitation spectrum $A(\boldsymbol{k}, \omega)$ and the $\boldsymbol{k}$-integrated spectrum $A(\omega)$ are shown in Fig. 5. The $4f$ peaks near E_F in the DFT result [Fig. 3(b)] are moved away from E_F in the presence of interactions. The peak at -1.9 eV corresponds to electron removal from the $j = 5/2$ multiplet of the $4f^1$ configuration ($4f^0$ final state), and the peak at 3.1 eV corresponds to electron addition and the final state is the $J = 4$ multiplet of the $4f^2$ configuration. The resultant energy dispersion near E_F is similar to LaB$_6$ [63,98]. A parabolic band around the X point forms a Fermi surface that is connected. The occupied part of our spectral function, Fig. 5(a), agrees very well with photoemission experiment [99] and is therefore a good starting point for the determination of two-particle quantities.
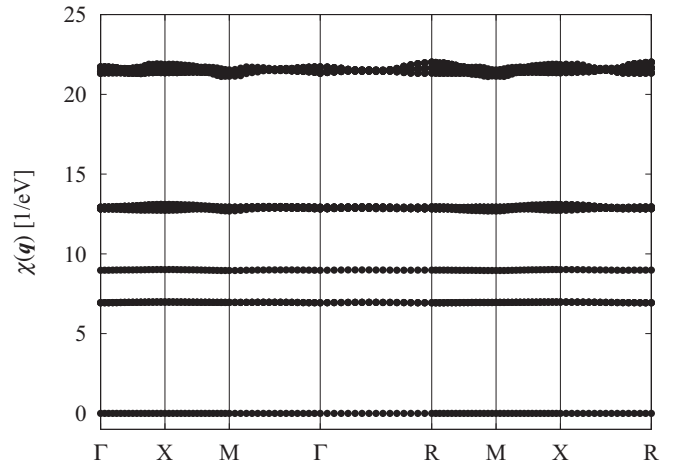

FIG. 6. The $\boldsymbol{q}$ dependence of 36 eigenvalues of the susceptibility matrix $\hat{\chi}(\boldsymbol{q})$ in the $j = 5/2$ states. $T = 0.01$ eV.

III. TWO-PARTICLE PROPERTIES

A. Multipolar susceptibility

The static susceptibility describing fluctuations within $j = 5/2$ states is given by

$$\chi_{m_1 m_2, m_3 m_4}(\boldsymbol{q}) = \int_0^\beta d\tau \langle O_{m_1 m_2}(\boldsymbol{q}, \tau) O_{m_4 m_3}(-\boldsymbol{q}) \rangle. \quad (3)$$

Here, the argument τ stands for the Heisenberg operator. The operator $O_{mm'}(\boldsymbol{q})$ is the Fourier transform of the local density operator defined by

$$O_{mm'}(i) = f_{im}^\dagger f_{im'}, \quad (4)$$

where $f_{im}^\dagger$ and f_{im} are the creation and annihilation operator for f electrons, respectively. The subscript m stands for the eigenvalues of j_z, namely, $m = -5/2, -3/2, \ldots, +5/2$. Therefore, there are $6^2 = 36$ components in the density operators, and $36^2 = 1296$ components in the susceptibility. Regarding $O_{mm'}$ as a vector, $\chi_{m_1 m_2, m_3 m_4}$ can be regarded as a (36×36) matrix, which we denote by $\hat{\chi}(\boldsymbol{q})$.

In DMFT, $\hat{\chi}(\boldsymbol{q})$ can be computed by solving the BS equation of the two-particle Green's function [1,100]. The two-particle Green's function depends on two fermionic Matsubara frequencies in addition to four m indices. We introduced a cutoff $\omega_{\max}$ for the frequency and solved the matrix equation of size $(36 N_\omega \times 36 N_\omega)$, where N_ω is the number of Matsubara frequencies below $\omega_{\max}$. All figures presented hereafter are results computed with $N_\omega = 160$ at $T = 0.01$ eV ($\omega_{\max} \approx 5.1$ eV), unless otherwise specified. For quantitative discussions, we extrapolate results to $\omega_{\max} \to \infty$ using results computed with up to $N_\omega = 400$.

Figure 6 shows the eigenvalues of the susceptibility matrix. There are 36 eigenvalues, which are classified into five groups. The leading group contains $15 = 4^2 - 1$ eigenvalues, which correspond to multipolar fluctuations within Γ_8 quartet states. The second group contains 16 eigenvalues, which arise due to mixing between Γ_8 and Γ_7 states (two times 4×2). The third largest is the single fluctuation mode with A_{1g} symmetry (hexadecapole). The fourth largest (second smallest) eigenvalues group contains $3 = 2^2 - 1$ fluctuation modes, which

TABLE II. The basis functions of 15 multipoles in the Γ_8 quartet system classified by the rank and irreducible representations (irreps). Extracted from Ref. [49].

	Irrep	Basis
Dipole	Γ_{4u}	$\{x,\ y,\ z\}$
Quadrupole	Γ_{3g}	$\{3z^2 - r^2,\ \sqrt{3}(x^2 - y^2)\}$
	Γ_{5g}	$\{xy,\ yz,\ zx\}$
Octupole	Γ_{2u}	xyz
	Γ_{4u}	$\{x(5x^2 - 3r^2),\ y(5y^2 - 3r^2),\ z(5z^2 - 3r^2)\}$
	Γ_{5u}	$\{x(y^2 - z^2),\ y(z^2 - x^2),\ z(x^2 - y^2)\}$

correspond to the spin fluctuations within Γ_7 doublet states. The lowest (almost zero) single-mode fluctuation is the charge fluctuation.

The eigenvectors of the susceptibility matrix yield multipoles that take the crystal symmetry into account. Instead, we can take linear combinations of $O_{mm'}$ using precomputed coefficients $C_{mm'}^{(\gamma)}$, namely,

$$O_\gamma = \sum_{mm'} C_{mm'}^{(\gamma)} O_{mm'}, \tag{5}$$

where the index γ distinguishes the irreducible representations. In point group O_h, 15 operators in the Γ_8 quartet system (excluding the charge) are classified into six kinds of multipoles according to the rank and irreducible representations [49,65,101]. Table II summarizes the basis function of these multipoles. The corresponding expressions for $C_{mm'}^{(\gamma)}$ can be constructed from the basis set [49,65,101]. We adopted a normalization $\sum_{mm'} |C_{mm'}^{(\gamma)}|^2 = 1$. The multipolar susceptibilities $\chi_\gamma(\boldsymbol{q})$ can then be evaluated by taking linear combinations of $\chi_{m_1 m_2, m_3 m_4}(\boldsymbol{q})$ according to

$$\chi_\gamma(\boldsymbol{q}) = \sum_{m_1 m_2 m_3 m_4} C_{m_1 m_2}^{(\gamma)} \chi_{m_1 m_2, m_3 m_4}(\boldsymbol{q}) C_{m_3 m_4}^{(\gamma)*}. \tag{6}$$

Other two-particle quantities having four indices are transformed into the multipolar basis γ in a similar manner.
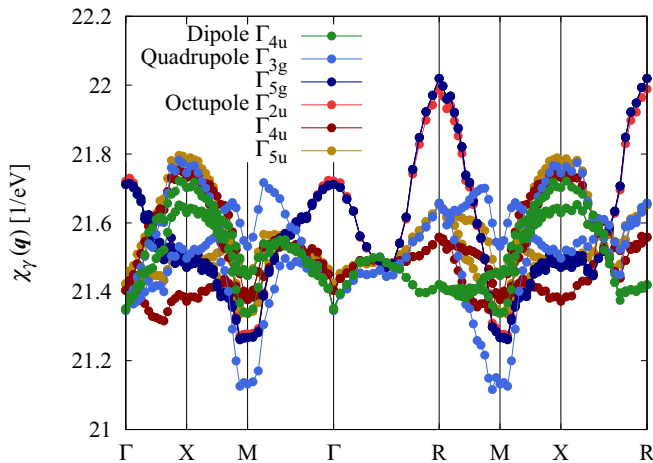

FIG. 7. The $\boldsymbol{q}$ dependence of 15 multipolar susceptibilities $\chi_\gamma(\boldsymbol{q})$ within Γ_8 states.

Figure 7 shows 15 susceptibilities $\chi_\gamma(\boldsymbol{q})$ within the Γ_8 states. The leading fluctuations are the quadrupoles of Γ_{5g} symmetry at the R point $[\boldsymbol{q} = (1/2, 1/2, 1/2) \equiv \boldsymbol{q}_R]$. This is consistent with the AFQ order of phase II in CeB$_6$. The second largest fluctuation is the octupole fluctuation of Γ_{2u} type, which is almost degenerate with the leading quadrupolar fluctuation. We will discuss this degeneracy later in the context of the multipolar interactions.

In order to determine the transition temperature, we need to decrease T to detect a divergence of $\chi_\gamma(\boldsymbol{q})$ (see for example Ref. [23]). However, it is practically difficult to perform the computations down to the expected transition temperature of order 1–10 K because the required number of Matsubara frequencies, N_ω, grows in inverse proportion to T. Hence, we adopt another strategy, namely, of extracting the effective intersite interactions. In the next two sections, we evaluate the intersite multipolar interactions using two different approaches.

B. Multipolar interactions (BS equation)

If the $4f$ electrons are well localized, we expect that a description using an effective Heisenberg-type model with multipolar degrees of freedom is a reasonable approximation. In this case, $\hat{\chi}(\boldsymbol{q})$ computed by solving the BS equation follows the form $\hat{\chi}(\boldsymbol{q}) \approx [\hat{\chi}_{\text{loc}}^{-1} - \hat{I}(\boldsymbol{q})]^{-1}$, since DMFT treats intersite correlations at a mean-field level. Here, $\hat{\chi}_{\text{loc}}$ is the local susceptibility evaluated in the effective impurity model. Assuming this expression, we define the effective intersite interaction $\hat{I}(\boldsymbol{q})$ by

$$\hat{I}(\boldsymbol{q}) \equiv \hat{\chi}_{\text{loc}}^{-1} - \hat{\chi}(\boldsymbol{q})^{-1}. \tag{7}$$

Once $\hat{I}(\boldsymbol{q})$ is obtained, we can extrapolate $\hat{\chi}(\boldsymbol{q})$ to lower temperatures because the dominant temperature dependence arises from $\hat{\chi}_{\text{loc}} \propto 1/T$ in localized $4f$ electron systems. We note that in the actual evaluation of $\hat{I}(\boldsymbol{q})$, the charge fluctuation has to be eliminated to avoid numerical instability in the matrix inversion (see Appendix B for details). The multipolar interactions $I_\gamma(\boldsymbol{q})$ are evaluated by performing the basis transformation from $\hat{I}(\boldsymbol{q})$ as in Eq. (6).

Figure 8 shows the multipolar interactions $I_\gamma(\boldsymbol{q})$ plotted separately for each irreducible representation. Here, positive (negative) values enhance (suppress) the fluctuations. The largest interaction is the quadrupole of Γ_{5g} type at the R point [Fig. 8(c)], which induces the AFQ order in phase II. We express this AFQ interaction by $I_Q(\boldsymbol{q}_R)$. Figure 8 indicates that the interaction strength of $I_Q(\boldsymbol{q}_R)$ is about 1 meV. An extrapolation to $\omega_{\text{max}} \to \infty$ yields $I_Q(\boldsymbol{q}_R) \approx 1.9$ meV (see Appendix C for details).

The transition temperature can be determined from the divergence of the susceptibility $\hat{\chi}(\boldsymbol{q}) = [\hat{\chi}_{\text{loc}}^{-1} - \hat{I}(\boldsymbol{q})]^{-1}$. At the high-symmetry $\boldsymbol{q}$ points, the criterion of the divergence is equivalent to the condition

$$\chi_{\text{loc},\gamma} I_\gamma(\boldsymbol{q}) = 1, \tag{8}$$

where $\chi_{\text{loc},\gamma}$ is the local multipolar susceptibility evaluated from $\hat{\chi}_{\text{loc}}$ [see Eq. (6)]. Figure 9 shows the temperature dependence of $\chi_{\text{loc},\gamma}$ within the Hubbard-I approximation. Since there is no γ dependence of $\chi_{\text{loc},\gamma}$, we hereafter omit the index γ and simply write it as χ_{loc}. The two lines in
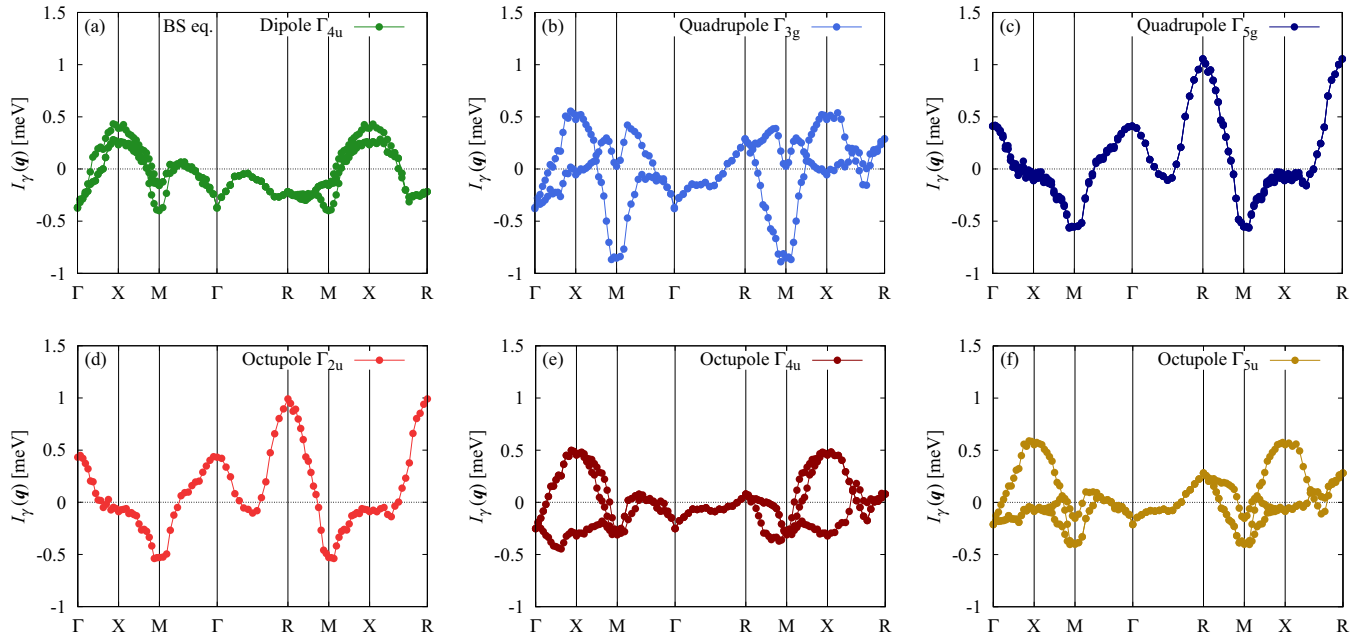
FIG. 8. The $\boldsymbol{q}$ dependence of the multipolar interactions $I_\gamma(\boldsymbol{q})$ within Γ_8 states computed by Eq. (7). Six kinds of multipoles are plotted separately. From (a)–(f) correspond to top to bottom in Table II.

Fig. 9 exhibit fits by the Curie-Weiss law $\chi_6 = C_6/(T - \Theta)$ for $T \gtrsim \Delta_{\mathrm{CEF}} = 11.3$ meV and the Curie law $\chi_4 = C_4/T$ for $T \lesssim \Delta_{\mathrm{CEF}}$. The coefficients are obtained as $C_6 = 0.169 \approx 1/6$ and $C_4 = 0.245 \approx 1/4$ as expected from the value of the (pseudo)degeneracy of the $4f^1$ configuration. Using the low-temperature behavior $\chi_{\mathrm{loc}} \approx 1/4T$ and assuming $I_\gamma(\boldsymbol{q})$ to be temperature independent in Eq. (8), we obtain an estimate of the transition temperature for the Γ_5-type AFQ order as $T_{\mathrm{Q}} \approx I_{\mathrm{Q}}(\boldsymbol{q}_{\mathrm{R}})/4 \approx 0.48$ meV $= 5.6$ K. This is consistent with the experimental value $T_{\mathrm{Q}} = 3.4$ K. The temperature dependence of $I_\gamma(\boldsymbol{q})$ will be discussed in Sec. III C.
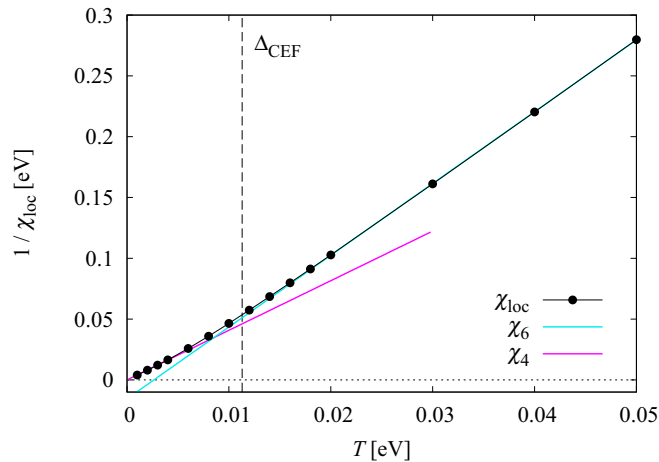

FIG. 9. Temperature dependence of the local susceptibility χ_{loc}. The two lines show $\chi_6 = C_6/(T - \Theta)$ with $C_6 = 0.169 \approx 1/6$ and $\Theta = 0.00316$ eV, and $\chi_4 = C_4/T$ with $C_4 = 0.245 \approx 1/4$. The dashed vertical line marks the energy of the CEF splitting $\Delta_{\mathrm{CEF}} = 0.0113$ eV.

The second largest interaction is the octupole of Γ_{2u} type [Fig. 8(d)]. This result is consistent with the general conclusion in Ref. [66]: "If the AFQ interaction of Γ_{5g} type is strong, the antiferro-octupolar interaction of Γ_{2u} type is equally strong." The Γ_{2u}-type antiferro-octupolar interaction plays a relevant role in stabilizing the AFQ ordering in phase II under magnetic field [49,65].

The order parameter in phase IV is reported as the octupole of Γ_{5u} type with $\boldsymbol{q} = \boldsymbol{q}_{\mathrm{R}}$ [49]. Our result shows that the octupolar interaction of Γ_{5u} type is largest at the X point and second largest at the R point. Hence, the interaction for phase IV is not relevant in pure CeB$_6$ without La substitution.

C. Multipolar interactions (SCL formula)

So far, we employed the BS equation, which requires an evaluation of the two-particle Green's function in the effective impurity model and subsequent large-scale matrix calculations. Here, we test a recently developed approximate method named strong-coupling-limit (SCL) formula [73]. In the following, we first review the SCL formula and then apply it to CeB$_6$.

In the SCL approximation, the momentum-dependent static susceptibility $\hat{\chi}(\boldsymbol{q})$ is given by

$$\hat{\chi}(\boldsymbol{q}) = \left[\hat{\chi}_{\mathrm{loc}}^{-1} - \hat{I}_{\mathrm{SCL}}(\boldsymbol{q}) \right]^{-1}, \qquad (9)$$

where $\hat{I}_{\mathrm{SCL}}(\boldsymbol{q})$ is the intersite interaction defined by

$$\hat{I}_{\mathrm{SCL}}(\boldsymbol{q}) = T \sum_n \phi(i\omega_n)^2 \hat{\Lambda}(i\omega_n, \boldsymbol{q}). \qquad (10)$$

The function $\hat{\Lambda}(i\omega_n, \boldsymbol{q})$ takes the energy dispersion into account and is given by

$$\hat{\Lambda}(i\omega_n, \boldsymbol{q}) = \hat{X}_{0,\mathrm{loc}}(i\omega_n)^{-1} - \hat{X}_0(i\omega_n, \boldsymbol{q})^{-1}, \qquad (11)$$
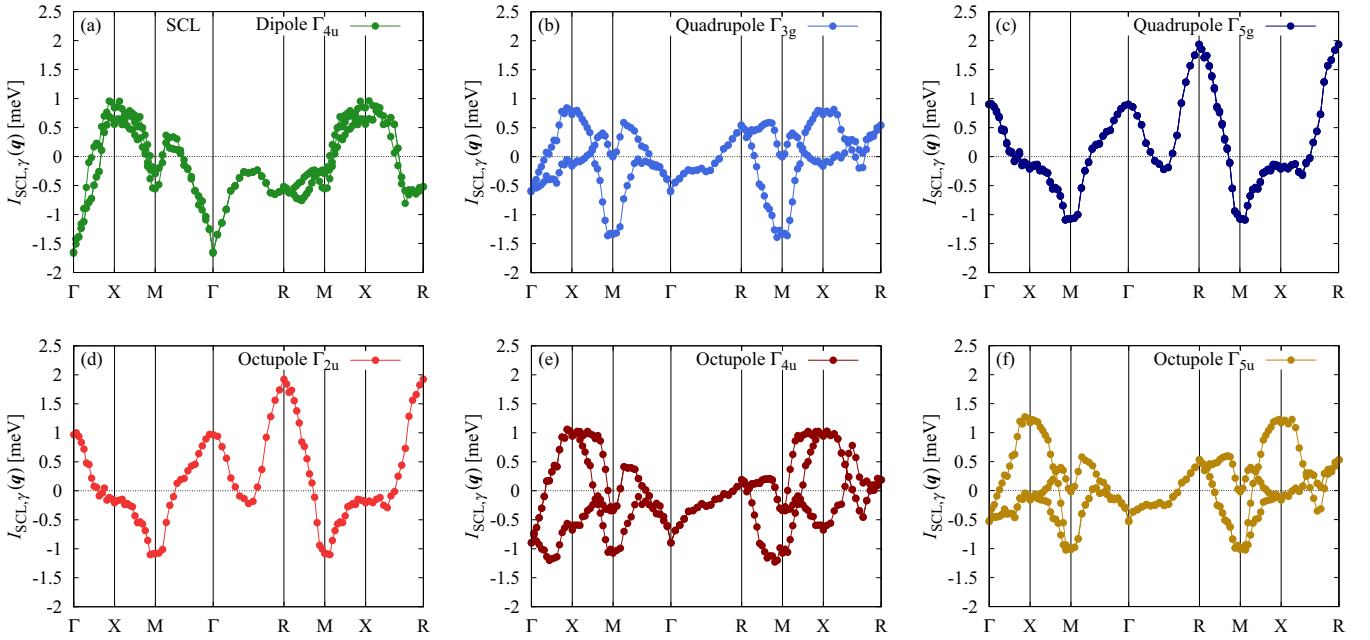
FIG. 10. The $\boldsymbol{q}$ dependence of the multipolar interactions $I_{\mathrm{SCL},\gamma}(\boldsymbol{q})$ within the Γ_8 states computed by the SCL formula. See the caption of Fig. 8 for further details.

where $\hat{X}_{0,\mathrm{loc}}(i\omega_n)$ and $\hat{X}_0(i\omega_n, \boldsymbol{q})$ are the bare two-particle Green's functions defined by

$$[\hat{X}_0(i\omega_n, \boldsymbol{q})]_{m_1 m_2, m_3 m_4}$$
$$= -N^{-1} \sum_{\boldsymbol{k}} G_{m_3 m_1}(\boldsymbol{k}, i\omega_n) G_{m_2 m_4}(\boldsymbol{k}+\boldsymbol{q}, i\omega_n), \quad (12)$$

and $\hat{X}_{0,\mathrm{loc}}(i\omega_n) = N^{-1} \sum_{\boldsymbol{q}} \hat{X}_0(i\omega_n, \boldsymbol{q})$ with N being the number of sites. On the other hand, the function $\phi(i\omega_n)$ takes the local fluctuations into account, which are described by the two-particle Green's function in the case of the BS equation. In Eq. (10), we neglected the orbital dependence of $\phi(i\omega_n)$. In the strong-coupling regime, $\phi(i\omega_n)$ is well approximated by the two-pole function

$$\phi(i\omega_n) = \frac{1}{i\omega_n + \Delta_-} - \frac{1}{i\omega_n - \Delta_+}, \quad (13)$$

where Δ_- and Δ_+ are the excitation energies from the $4f^n$ state ($n = 1$ for the Ce^{3+} ion) to $4f^{n-1}$ and $4f^{n+1}$ states, respectively (see Sec. II B). The two-pole approximation corresponds to neglecting the multiplet structure in the excited $4f^{n\pm1}$ states. By using Eq. (13), we can evaluate $\hat{I}_{\mathrm{SCL}}(\boldsymbol{q})$ and $\hat{\chi}(\boldsymbol{q})$ without computing the two-particle Green's function and hence no extra cost of solving the effective impurity problem is incurred. This approximation was specifically termed SCL3 in Ref. [73]. It has been proven analytically that $\hat{I}_{\mathrm{SCL}}(\boldsymbol{q})$ is reduced to the RKKY interaction or the superexchange interaction in the strong-coupling limit when it is applied to the periodic Anderson model or the Hubbard model, respectively [73]. We use $\Delta_- = 1.9\,\mathrm{eV}$ and $\Delta_+ = 3.1\,\mathrm{eV}$ as presented in Table I.

Figure 10 shows the multipolar interactions $I_{\mathrm{SCL},\gamma}(\boldsymbol{q})$ computed using the SCL formula [the transformation to the multipolar basis γ was taken as in Eq. (6)]. It turns out that, apart from the scale of the vertical axis, the overall structure

is the same as that obtained by the BS equation (Fig. 8). In particular, the largest interaction of the Γ_{5g} quadrupole at the R point [Fig. 10(c)] and the second largest interaction of the Γ_{2u} octupole [Fig. 10(d)] are correctly reproduced. The magnitude of the Γ_{5g} quadrupole interaction at the R point is $I_{\mathrm{Q}}(\boldsymbol{q}_{\mathrm{R}}) \approx 1.93\,\mathrm{meV}$, which is in surprisingly good agreement with the value obtained after extrapolation to $\omega_{\max} \to \infty$ in the BS equation. This result demonstrates that the SCL formula is valid not only in model calculations as shown in Ref. [73] but also in realistic material calculations.

At the end of this section, we discuss the temperature dependence of the multipolar interactions. Figure 11 shows the temperature dependence of $I_{\mathrm{SCL},\gamma}(\boldsymbol{q}_{\mathrm{R}})$ for multipoles γ that have positive interaction values (that enhance fluctuations). The results down to $T = 0.008\,\mathrm{eV}$ are plotted. For
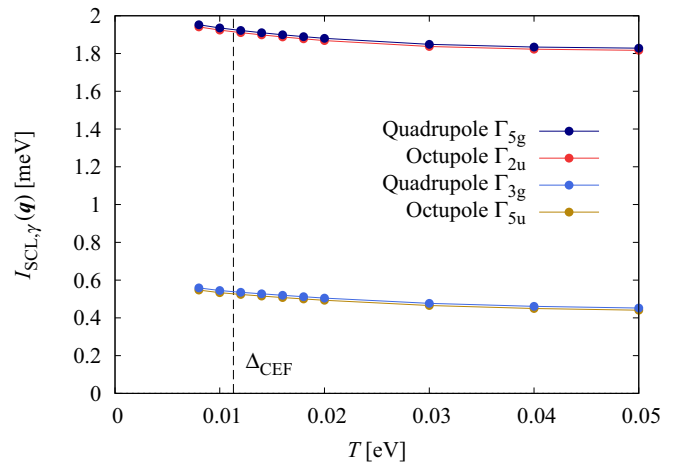

FIG. 11. Temperature dependence of the multipolar interactions $I_{\mathrm{SCL},\gamma}(\boldsymbol{q}_{\mathrm{R}})$. The dashed vertical line marks the energy of the CEF splitting $\Delta_{\mathrm{CEF}} = 0.0113\,\mathrm{eV}$.
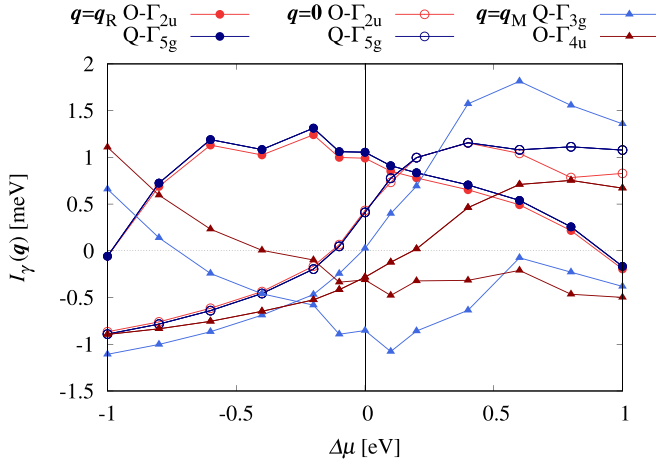
FIG. 12. Variations of relevant effective interactions $I_\gamma(\boldsymbol{q})$ against the shift of the chemical potential, $\Delta\mu$. $I_\gamma(\boldsymbol{q})$ was computed by Eq. (7). The symbols indicate the $\boldsymbol{q}$ vector: closed circles for the R point, open circles for the Γ point, and closed triangles for the M point.

$T \lesssim 0.006$ eV, we could not take enough Matsubara frequencies to achieve convergence. Within the computed range of temperatures, $I_{\mathrm{SCL},\gamma}(\boldsymbol{q}_{\mathrm{R}})$ gradually increases with decreasing temperature. This behavior is consistent with the result in the Hubbard model [73]. We thus confirm that the dominant T dependence in $\chi_\gamma(\boldsymbol{q})$ originates from χ_{loc}, which grows in proportion to $1/T$.

IV. DOPING DEPENDENCE

In order to clarify which energy band plays a major role in the experimental quadrupolar ordering, we artificially shift the chemical potential and investigate how the effective interactions $I_\gamma(\boldsymbol{q})$ vary. Such a numerical experiment is one of the advantages of theoretical calculations. We shifted the chemical potential by up to ± 1 eV in a rigid band treatment. The shift of the chemical potential changes the electron number per unit cell by -0.6 for $\Delta\mu = -1$ eV and $+0.9$ for $\Delta\mu = +1$ eV, while the $4f$ electron number is unchanged. Therefore, electron (hole) doping per boron is 0.15 (0.10) at $\Delta\mu = +1$ eV (-1 eV). The Fermi surface changes as follows: Under the hole doping, the open Fermi surface centered at the X point closes (the dispersion on the Γ-M line in Fig. 5 moves away from E_{F}). On the other hand, the electron doping generates small electron pockets on the Γ-M line, and hence another contribution to the susceptibility is expected.

Figure 12 shows the variation of the effective interactions $I_\gamma(\boldsymbol{q})$ as a function of $\Delta\mu$. We plotted only relevant interactions: the Γ_{5g} quadrupole and the Γ_{2u} octupole at R point and Γ point, and the Γ_{3g} quadrupole and the Γ_{4u} octupole at the M point. The leading interaction $I_Q(\boldsymbol{q}_{\mathrm{R}})$ for $\Delta\mu = 0$ is enhanced by the hole doping ($\Delta\mu < 0$). Therefore, we conclude that the Fermi surface around the X point causes the experimental quadrupolar ordering. Upon further hole doping, the octupolar interaction of Γ_{4u} type becomes dominant.

On the other hand, $I_Q(\boldsymbol{q}_{\mathrm{R}})$ is suppressed by electron doping ($\Delta\mu > 0$), which leads to a reduction of the transition temperature of phase II. Instead, the same multipole with

a different $\boldsymbol{q}$ vector, namely, the Γ_{5g}-type ferroquadrupolar interaction $I_Q(\boldsymbol{0})$ is enhanced. Upon further electron doping, the quadrupolar interaction of Γ_{3g} type at the M point takes the place of the leading interaction. Our theory thus predicts that the quadrupolar order in phase II is robust against hole doping but is replaced by other order parameters upon electron doping.

V. SUMMARY

We demonstrated a microscopic derivation of multipolar ordering using the DFT+DMFT method. There are three parameters in these calculations: U, J_{H}, and $\Delta\epsilon_f$. We showed a recipe to fix them: ϵ_f is determined from the PES spectrum, and $U - J_{\mathrm{H}}$ can be determined from the BIS spectrum. By fixing J_{H} to a typical value, we can thus determine these parameters in an unbiased manner.

We evaluated the $\boldsymbol{q}$-dependent multipolar susceptibilities and interactions in CeB_6 by solving the Bethe-Salpeter equation and by using the SCL formula. The SCL formula, which does not require the evaluation of the two-particle Green's function, is shown to provide reasonable results that are comparable to the $\omega_{\max} \to \infty$ limit of the BS equation. Although direct observation of the second-order phase transition is practically difficult at present, we can estimate the transition temperature by extrapolating the susceptibility to low temperatures. Our results yield a good estimate.

Comparing our approach to the more traditional combination of multiorbital Kondo lattice model and RKKY formula, there are a few advantages to the new method: (i) We base our calculations on the full DFT+DMFT spectral function so that the validity of our calculation can already be checked at the single-particle level by comparing to photoemission spectroscopy experiment. (ii) Our approach is free from highly compound specific parameters that need to be determined from experiment; with only two local interaction parameters U and J_{H} and a binding energy of the single f electron, the method can be applied to numerous Ce compounds. (iii) Our calculation procedure based on the DFT+DMFT method is not limited to highly localized f electron systems but can be also applied to itinerant f electron systems. The only difference to the calculations in this paper is the impurity solver: We have to use more sophisticated impurity solvers such as the continuous-time quantum Monte Carlo method [95] to incorporate the formation of heavy-fermion states. Interesting applications include a hidden order in URu_2Si_2 and scalar order in $PrFe_4P_{12}$ [49]. These are two of the many possible future uses of our method.

APPENDIX A: DETERMINATION OF PARAMETERS U, J_{H}, AND $\Delta\epsilon_f$

We present the procedure of determining three parameters U, J_{H}, and $\Delta\epsilon_f$ so that Δ_- and Δ_+ agree with the target values. We first vary $\Delta\epsilon_f$ with U and J_{H} fixed at 6.0 eV and
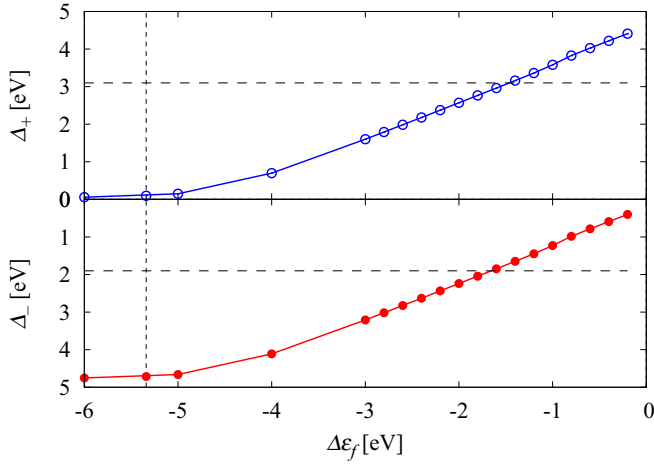
FIG. 13. Calculated Δ_- and Δ_+ as a function of $\Delta\epsilon_f$ for $U = 6.0$ eV and $J_H = 0.8$ eV. The horizontal dashed lines indicate the target values, $\Delta_- = 1.9$ eV and $\Delta_+ = 3.1$ eV. The vertical dashed line indicates the value of $\Delta\epsilon_f$ estimated by the Hartree energy.

FIG. 14. Extrapolation to $\omega_{\max} \to \infty$ ($1/\omega_{\max} \to 0$) for the four leading effective interactions $I_\gamma(q_R)$ computed by the BS equation. The dashed lines show the result of linear fitting.

0.8 eV. Figure 13 shows Δ_- and Δ_+ as a function of $\Delta\epsilon_f$. The lower graph for Δ_- is plotted with an inverted y axis because of the definition $\Delta_- = -E_1$. We find that the target value $\Delta_- = 1.9$ eV is obtained at $\Delta\epsilon_f = -1.6$ eV. For information, when we estimate $\Delta\epsilon_f$ from the Hartree energy, we obtained $\Delta\epsilon_f \approx -5.3$ eV, which yields an unphysically deep $4f$ level.

Next, we turn our attention to Δ_+. The sum $\Delta_- + \Delta_+$ [the difference between $4f^1$ and $4f^2$ peaks in $A(\omega)$] depends on $U - J_H$, because Δ_+ is the excitation energy from E_F to the Hund ground state of the $4f^2$ configuration. While the difference between U and J_H is thus determined, there is still one freedom in setting U or J_H. Following Ref. [93], we fix $J_H = 0.8$ eV and vary U. Then, we found that $U = 6.2$ eV gives the target value $\Delta_+ = 3.1$ eV.

APPENDIX B: CALCULATION OF THE EFFECTIVE INTERACTION

Direct calculation of Eq. (7) is unstable because the charge fluctuation is tiny (or zero within the computer accuracy) and the inversions of the matrices $\hat{\chi}_{loc}$ and $\hat{\chi}(q)$ diverge. Actually, these divergences are canceled out to yield a finite result for $\hat{I}(q)$. We present here how to avoid this instability.

We decompose $\hat{\chi}_{loc}$ using the singular value decomposition (SVD). Since $\hat{\chi}_{loc}$ is Hermitian, SVD is reduced to diagonalization
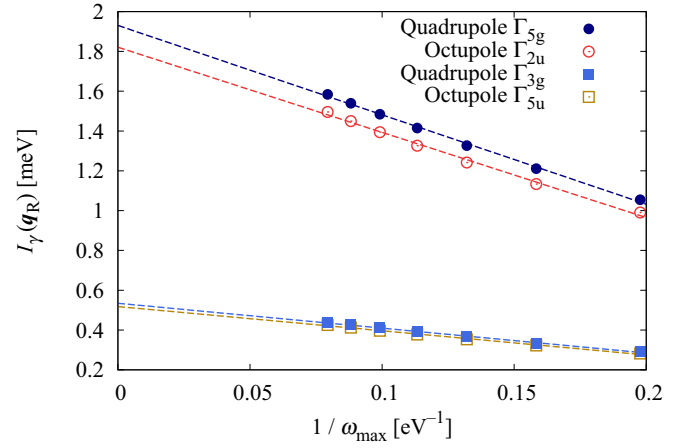
$$\hat{\chi}_{loc} = USU^\dagger, \tag{B1}$$

where U is a unitary matrix, and S is a diagonal matrix whose diagonal elements (singular values) are positive and aligned in descending order. It is clear from the above expression that small singular values make the matrix inversion unstable. Suppose that the smallest singular value is zero, then we eliminate it and the corresponding basis from U. In this singular space, S and U are replaced, respectively, with an $[(M-1) \times (M-1)]$ diagonal matrix $\tilde{S}$ and $[M \times (M-1)]$ matrix $\tilde{U}$. Eq. (7) is then expressed as

$$\hat{I}(q) \simeq \tilde{U}[\tilde{S}^{-1} - (\tilde{U}^\dagger \hat{\chi}(q)\tilde{U})^{-1}]\tilde{U}^\dagger. \tag{B2}$$

This expression does not suffer from numerical instability.

APPENDIX C: EXTRAPOLATION OF THE FREQUENCY CUTOFF

We solved the BS equation for $\chi(q)$ by introducing the cutoff $\omega_{\max}$ for the fermionic Matsubara frequency. In this Appendix, we present extrapolation to $\omega_{\max} \to \infty$. Figure 14 shows the effective interaction $I_\gamma(q_R)$ as a function of $1/\omega_{\max}$. Here, the results for $N_\omega = 160, 200, \ldots, 400$ are plotted. The data are well approximated by a line as indicated by the dashed lines. Thus, extrapolation to $1/\omega_{\max} \to 0$ yields $I_\gamma(q_R) \approx 1.93$ meV for the Γ_{5g}-type quadrupolar interaction.

More elaborate methods for solving the BS equation have been proposed [42,102–105]. These approaches make the convergence faster or may allow us to obtain converged results without extrapolation.

[1] A. Georges, G. Kotliar, W. Krauth, and M. J. Rozenberg, Dynamical mean-field theory of strongly correlated fermion systems and the limit of infinite dimensions, Rev. Mod. Phys. **68**, 13 (1996).

[2] G. Kotliar, S. Y. Savrasov, K. Haule, V. S. Oudovenko, O. Parcollet, and C. A. Marianetti, Electronic structure calculations with dynamical mean-field theory, Rev. Mod. Phys. **78**, 865 (2006).

[3] M. Imada and T. Miyake, Electronic structure calculation by first principles for strongly correlated electron systems, J. Phys. Soc. Jpn. **79**, 112001 (2010).

[4] K. Held, Electronic structure calculations using dynamical mean field theory, Adv. Phys. **56**, 829 (2007).

[5] E. Gorelov, M. Karolak, T. O. Wehling, F. Lechermann, A. I. Lichtenstein, and E. Pavarini, Nature of the Mott transition in Ca$_2$RuO$_4$, Phys. Rev. Lett. **104**, 226401 (2010).

[6] S. Backes, T. C. Rödel, F. Fortuna, E. Frantzeskakis, P. Le Fèvre, F. Bertran, M. Kobayashi, R. Yukawa, T. Mitsuhashi, M. Kitamura, K. Horiba, H. Kumigashira, R. Saint-Martin, A. Fouchet, B. Berini, Y. Dumont, A. J. Kim, F. Lechermann, H. O. Jeschke, M. J. Rozenberg *et al.*, Hubbard band versus oxygen vacancy states in the correlated electron metal SrVO$_3$, Phys. Rev. B **94**, 241110(R) (2016).

[7] C. Ahn, A. Cavalleri, A. Georges, S. Ismail-Beigi, A. J. Millis, and J.-M. Triscone, Designing and controlling the properties of transition metal oxide quantum materials, Nat. Mater. **20**, 1462 (2021).

[8] M. Aichhorn, L. Pourovskii, V. Vildosola, M. Ferrero, O. Parcollet, T. Miyake, A. Georges, and S. Biermann, Dynamical mean-field theory within an augmented plane-wave framework: Assessing electronic correlations in the iron pnictide LaFeAsO, Phys. Rev. B **80**, 085101 (2009).

[9] Z. P. Yin, K. Haule, and G. Kotliar, Magnetism and charge dynamics in iron pnictides, Nat. Phys. **7**, 294 (2011).

[10] J. Ferber, H. O. Jeschke, and R. Valentí, Fermi surface topology of LaFePO and LiFeP, Phys. Rev. Lett. **109**, 236403 (2012).

[11] K. Haule, C.-H. Yee, and K. Kim, Dynamical mean-field theory within the full-potential methods: Electronic structure of CeIrIn$_5$, CeCoIn$_5$, and CeRhIn$_5$, Phys. Rev. B **81**, 195107 (2010).

[12] H. Lu and L. Huang, Pressure-driven $4f$ localized-itinerant crossover in heavy-fermion compound CeIn$_3$: A first-principles many-body perspective, Phys. Rev. B **94**, 075132 (2016).

[13] H. Ebert, D. Ködderitzsch, and J. Minár, Calculating condensed matter properties using the KKR-Green's function method—recent developments and applications, Rep. Prog. Phys. **74**, 096501 (2011).

[14] G. Rohringer, H. Hafermann, A. Toschi, A. A. Katanin, A. E. Antipov, M. I. Katsnelson, A. I. Lichtenstein, A. N. Rubtsov, and K. Held, Diagrammatic routes to nonlocal correlations beyond dynamical mean field theory, Rev. Mod. Phys. **90**, 025003 (2018).

[15] R. Sakuma, P. Werner, and F. Aryasetiawan, Electronic structure of SrVO$_3$ within $GW + $ DMFT, Phys. Rev. B **88**, 235110 (2013).

[16] J. M. Tomczak, M. Casula, T. Miyake, and S. Biermann, Asymmetry in band widening and quasiparticle lifetimes in SrVO$_3$: Competition between screened exchange and local correlations from combined GW and dynamical mean-field theory $GW + $ DMFT, Phys. Rev. B **90**, 165138 (2014).

[17] Z. Y. Meng, Y. B. Kim, and H.-Y. Kee, Odd-parity triplet superconducting phase in multiorbital materials with a strong spin-orbit coupling: Application to doped Sr$_2$IrO$_4$, Phys. Rev. Lett. **113**, 177003 (2014).

[18] A. Galler, P. Thunström, P. Gunacker, J. M. Tomczak, and K. Held, *Ab initio* dynamical vertex approximation, Phys. Rev. B **95**, 115107 (2017).

[19] H. Lee, K. Foyevtsova, J. Ferber, M. Aichhorn, H. O. Jeschke, and R. Valentí, Dynamical cluster approximation within an augmented plane wave framework: Spectral properties of SrVO$_3$, Phys. Rev. B **85**, 165103 (2012).

[20] J. Kuneš, I. Leonov, P. Augustinský, V. Křápek, M. Kollar, and D. Vollhardt, LDA+DMFT approach to ordering phenomena

[21] A. I. Liechtenstein, M. Katsnelson, V. Antropov, and V. Gubanov, Local spin density functional approach to the theory of exchange interactions in ferromagnetic metals and alloys, J. Magn. Magn. Mater. **67**, 65 (1987).

[22] S. V. Halilov, H. Eschrig, A. Y. Perlov, and P. M. Oppeneer, Adiabatic spin dynamics from spin-density-functional theory: Application to Fe, Co, and Ni, Phys. Rev. B **58**, 293 (1998).

[23] A. I. Lichtenstein, M. I. Katsnelson, and G. Kotliar, Finite-temperature magnetism of transition metals: An *ab initio* dynamical mean-field theory, Phys. Rev. Lett. **87**, 067205 (2001).

[24] I. Leonov, A. I. Poteryaev, V. I. Anisimov, and D. Vollhardt, Electronic correlations at the α-γ structural phase transition in paramagnetic iron, Phys. Rev. Lett. **106**, 106405 (2011).

[25] A. S. Belozerov, I. Leonov, and V. I. Anisimov, Magnetism of iron and nickel from rotationally invariant Hirsch-Fye quantum Monte Carlo calculations, Phys. Rev. B **87**, 125138 (2013).

[26] A. Szilva, M. Costa, A. Bergman, L. Szunyogh, L. Nordström, and O. Eriksson, Interatomic exchange interactions for finite-temperature magnetism and nonequilibrium spin dynamics, Phys. Rev. Lett. **111**, 127204 (2013).

[27] T. Nomoto, T. Koretsune, and R. Arita, Local force method for the *ab initio* tight-binding model: Effect of spin-dependent hopping on exchange interactions, Phys. Rev. B **102**, 014444 (2020).

[28] W. E. Pickett, A. J. Freeman, and D. D. Koelling, Local-density-functional approach to the isostructual γ-α transition in cerium using the self-consistent linearized-augmented-plane-wave method, Phys. Rev. B **23**, 1266 (1981).

[29] K. Held, A. K. McMahan, and R. T. Scalettar, Cerium volume collapse: Results from the merger of dynamical mean-field theory and local density approximation, Phys. Rev. Lett. **87**, 276404 (2001).

[30] A. K. McMahan, K. Held, and R. T. Scalettar, Thermodynamic and spectral properties of compressed Ce calculated using a combined local-density approximation and dynamical mean-field theory, Phys. Rev. B **67**, 075108 (2003).

[31] O. Sakai, Y. Shimizu, and Y. Kaneta, Band calculation for Ce-Compounds on the basis of dynamical mean field theory, J. Phys. Soc. Jpn. **74**, 2517 (2005).

[32] N. Lanatà, Y.-X. Yao, C.-Z. Wang, K.-M. Ho, J. Schmalian, K. Haule, and G. Kotliar, $\gamma - \alpha$ isostructural transition in cerium, Phys. Rev. Lett. **111**, 196801 (2013).

[33] E. Pavarini, E. Koch, and A. I. Lichtenstein, Mechanism for orbital ordering in KCuF$_3$, Phys. Rev. Lett. **101**, 266405 (2008).

[34] J. Musshoff, G. Zhang, E. Koch, and E. Pavarini, Linear-response description of superexchange-driven orbital ordering in K$_2$CuF$_4$, Phys. Rev. B **100**, 045116 (2019).

[35] L. V. Pourovskii, Two-site fluctuations and multipolar intersite exchange interactions in strongly correlated systems, Phys. Rev. B **94**, 115117 (2016).

[36] L. V. Pourovskii and S. Khmelevskyi, Quadrupolar superexchange interactions, multipolar order, and magnetic phase transition in UO$_2$, Phys. Rev. B **99**, 094439 (2019).

[37] M. Matsumoto, M. J. Han, J. Otsuki, and S. Y. Savrasov, First-principles simulations of heavy Fermion cerium compounds

and the structural stability of correlated materials, Eur. Phys. J. Spec. Top. **226**, 2641 (2017).

based on the Kondo lattice, Phys. Rev. Lett. **103**, 096403 (2009).

[38] K. Haule and G. Kotliar, Arrested Kondo effect and hidden order in URu$_2$Si$_2$, Nat. Phys. **5**, 796 (2009).

[39] H. Shinaoka, S. Hoshino, M. Troyer, and P. Werner, Phase diagram of pyrochlore iridates: All-in–all-out magnetic ordering and non-Fermi-liquid properties, Phys. Rev. Lett. **115**, 156401 (2015).

[40] S. Mandal, K. Haule, K. M. Rabe, and D. Vanderbilt, Systematic beyond-DFT study of binary transition metal oxides, npj Comput. Mater. **5**, 115 (2019).

[41] H. Fujiwara, K. Terashima, J. Otsuki, N. Takemori, H. O. Jeschke, T. Wakita, Y. Yano, W. Hosoda, N. Kataoka, A. Teruya, M. Kakihana, M. Hedo, T. Nakama, Y. Ōnuki, K. Yaji, A. Harasawa, K. Kuroda, S. Shin, K. Horiba, H. Kumigashira *et al.*, Anomalously large spin-dependent electron correlation in the nearly half-metallic ferromagnet CoS$_2$, Phys. Rev. B **106**, 085114 (2022).

[42] J. Kuneš, Efficient treatment of two-particle vertices in dynamical mean-field theory, Phys. Rev. B **83**, 085102 (2011).

[43] Z. P. Yin, K. Haule, and G. Kotliar, Spin dynamics and orbital-antiphase pairing symmetry in iron-based superconductors, Nat. Phys. **10**, 845 (2014).

[44] H. U. R. Strand, M. Zingl, N. Wentzell, O. Parcollet, and A. Georges, Magnetic response of Sr$_2$RuO$_4$: Quasi-local spin fluctuations due to Hund's coupling, Phys. Rev. B **100**, 125120 (2019).

[45] D. Geffroy, J. Kaufmann, A. Hariki, P. Gunacker, A. Hausoel, and J. Kuneš, Collective modes in excitonic magnets: Dynamical mean-field study, Phys. Rev. Lett. **122**, 127601 (2019).

[46] J. H. Shim, K. Haule, and G. Kotliar, Modeling the localized-to-itinerant electronic transition in the heavy fermion system CeIrIn$_5$, Science **318**, 1615 (2007).

[47] J. Otsuki, H. Kusunose, and Y. Kuramoto, Evolution of a large Fermi surface in the Kondo lattice, Phys. Rev. Lett. **102**, 017202 (2009).

[48] J. Otsuki, Competing d-wave and p-wave spin-singlet superconductivities in the two-dimensional Kondo lattice, Phys. Rev. Lett. **115**, 036404 (2015).

[49] Y. Kuramoto, H. Kusunose, and A. Kiss, Multipole orders and fluctuations in strongly correlated electron systems, J. Phys. Soc. Jpn. **78**, 072001 (2009).

[50] E. Zirngiebl, B. Hillebrands, S. Blumenröder, G. Güntherodt, M. Loewenhaupt, J. M. Carpenter, K. Winzer, and Z. Fisk, Crystal-field excitations in CeB$_6$ studied by Raman and neutron spectroscopy, Phys. Rev. B **30**, 4052 (1984).

[51] T. Fujita, M. Suzuki, T. Komatsubara, S. Kunii, T. Kasuya, and T. Ohtsuka, Anomalous specific heat of CeB$_6$, Solid State Commun. **35**, 569 (1980).

[52] H. Nakao, K.-i. Magishi, Y. Wakabayashi, Y. Murakami, K. Koyama, K. Hirota, Y. Endoh, and S. Kunii, Antiferroquadrupole ordering of CeB$_6$ studied by resonant x-ray scattering, J. Phys. Soc. Jpn. **70**, 1857 (2001).

[53] Y. Tanaka, U. Staub, K. Katsumata, S. W. Lovesey, J. E. Lorenzo, Y. Narumi, V. Scagnoli, S. Shimomura, Y. Tabata, Y. Onuki, Y. Kuramoto, A. Kikkawa, T. Ishikawa, and H. Kitamura, Direct and quantitative determination of the orbital ordering in CeB$_6$ by X-ray diffraction, Europhys. Lett. **68**, 671 (2004).

[54] P. Y. Portnichenko, A. Akbari, S. E. Nikitin, A. S. Cameron, A. V. Dukhnenko, V. B. Filipov, N. Y. Shitsevalova, P. Čermák, I. Radelytskyi, A. Schneidewind, J. Ollivier, A. Podlesnyak, Z. Huesges, J. Xu, A. Ivanov, Y. Sidis, S. Petit, J.-M. Mignot, P. Thalmeier, and D. S. Inosov, Field-angle-resolved magnetic excitations as a probe of hidden-order symmetry in CeB$_6$, Phys. Rev. X **10**, 021010 (2020).

[55] T. Mito, H. Mori, K. Miyamoto, T. Tanaka, Y. Nakai, K. Ueda, F. Iga, and H. Harima, Symmetry analysis of zero-field antiferroquadrupole order in CeB$_6$: Extremely low-frequency ^{11}B-NQR study, J. Phys. Soc. Jpn. **92**, 034702 (2023).

[56] J. Effantin, J. Rossat-Mignod, P. Burlet, H. Bartholin, S. Kunii, and T. Kasuya, Magnetic phase diagram of CeB$_6$, J. Magn. Magn. Mater. **47-48**, 145 (1985).

[57] T. Tayama, T. Sakakibara, K. Tenya, H. Amitsuka, and S. Kunii, Magnetic phase diagram of Ce$_x$La$_{1-x}$B$_6$ studied by static magnetization measurement at very low temperatures, J. Phys. Soc. Jpn. **66**, 2268 (1997).

[58] K. Kubo and Y. Kuramoto, Octupole ordering model for the phase IV of Ce$_x$La$_{1-x}$B$_6$, J. Phys. Soc. Jpn. **73**, 216 (2004).

[59] D. Mannix, Y. Tanaka, D. Carbone, N. Bernhoeft, and S. Kunii, Order parameter segregation in Ce$_{0.7}$La$_{0.3}$B$_6$: 4f octopole and 5d dipole magnetic order, Phys. Rev. Lett. **95**, 117206 (2005).

[60] H. Kusunose and Y. Kuramoto, Evidence for octupole order in Ce$_{0.7}$La$_{0.3}$B$_6$ from resonant x-ray scattering, J. Phys. Soc. Jpn. **74**, 3139 (2005).

[61] S. Nakamura, T. Goto, and S. Kunii, Magnetic phase diagrams of the dense Kondo compounds CeB$_6$ and Ce$_{0.5}$La$_{0.5}$B$_6$, J. Phys. Soc. Jpn. **64**, 3941 (1995).

[62] F. J. Ohkawa, Orbital antiferromagnetism in CeB$_6$, J. Phys. Soc. Jpn. **54**, 3909 (1985).

[63] Y. Ōnuki, T. Komatsubara, P. H. P. Reinders, and M. Springford, Fermi surface and cyclotron mass of CeB$_6$, J. Phys. Soc. Jpn. **58**, 3698 (1989).

[64] R. Shiina, H. Shiba, and P. Thalmeier, Magnetic-field effects on quadrupolar ordering in a Γ_8-quartet system CeB$_6$, J. Phys. Soc. Jpn. **66**, 1741 (1997).

[65] R. Shiina, O. Sakai, H. Shiba, and P. Thalmeier, Interplay of field-induced multipoles in CeB$_6$, J. Phys. Soc. Jpn. **67**, 941 (1998).

[66] H. Shiba, O. Sakai, and R. Shiina, Nature of Ce-Ce interaction in CeB$_6$ and its consequences, J. Phys. Soc. Jpn. **68**, 1988 (1999).

[67] G. Sakurai and Y. Kuramoto, Multipolar interactions in the Anderson lattice with orbital degeneracy, J. Phys. Soc. Jpn. **73**, 225 (2004).

[68] G. Sakurai and Y. Kuramoto, Wavenumber dependence of multipolar interactions in the Anderson lattice, J. Phys. Soc. Jpn. **74**, 975 (2005).

[69] T. Yamada and K. Hanzawa, Derivation of RKKY interaction between multipole moments in CeB$_6$ by the effective Wannier model based on the bandstructure calculation, J. Phys. Soc. Jpn. **88**, 084703 (2019).

[70] K. Hanzawa and T. Yamada, Origin of anisotropic RKKY interactions in CeB$_6$, J. Phys. Soc. Jpn. **88**, 124710 (2019).

[71] K. Kubo and T. Hotta, Microscopic theory of multipole ordering in NpO$_2$, Phys. Rev. B **71**, 140404(R) (2005).

[72] Y. Iizuka, T. Yamada, K. Hanzawa, and Y. Ōno, First-principles study of the RKKY interaction and the quadrupole

order in the Pr 1-2-20 systems PrT_2Al_{20} ($T =$ Ti, V), J. Phys. Soc. Jpn. **91**, 074708 (2022).

[73] J. Otsuki, K. Yoshimi, H. Shinaoka, and Y. Nomura, Strong-coupling formula for momentum-dependent susceptibilities in dynamical mean-field theory, Phys. Rev. B **99**, 165134 (2019).

[74] K. Koepernik and H. Eschrig, Full-potential nonorthogonal local-orbital minimum-basis band-structure scheme, Phys. Rev. B **59**, 1743 (1999).

[75] K. Tanaka, Y. Kato, and Y. Onuki, $4f$-Electron density distribution in crystals of CeB_6 at 165 K and its analysis based on the crystal field theory, Acta Cryst. B **53**, 143 (1997).

[76] H. Eschrig and K. Koepernik, Tight-binding models for the iron-based superconductors, Phys. Rev. B **80**, 104503 (2009).

[77] K. Koepernik, O. Janson, Y. Sun, and J. van den Brink, Symmetry-conserving maximally projected Wannier functions, Phys. Rev. B **107**, 235135 (2023).

[78] T. Hotta, Spin and orbital structure of uranium compounds on the basis of a j-j coupling scheme, Phys. Rev. B **70**, 054405 (2004).

[79] T. Hotta and H. Harima, Effective crystalline electric field potential in a j-j coupling scheme, J. Phys. Soc. Jpn. **75**, 124711 (2006).

[80] V. I. Anisimov, F. Aryasetiawan, and A. I. Lichtenstein, First-principles calculations of the electronic structure and spectra of strongly correlated systems: the LDA + U method, J. Phys.: Condens. Matter **9**, 767 (1997).

[81] G. Chiaia, O. Tjernberg, S. Du'o, S. De Rossi, P. Vavassori, I. Lindau, T. Takahashi, S. Kunii, T. Komatsubara, D. Cocco, S. Lizzit, and G. Paolucci, CeB_6 and $CeCu_6$ single crystals probed by resonant photoemission spectroscopy: A comparison between the two electronic structures, Phys. Rev. B **55**, 9207 (1997).

[82] S. Souma, H. Kumigashira, T. Ito, T. Sato, T. Takahashi, and S. Kunii, Crystal-field splitting in CeB_6 observed by ultrahigh-resolution photoemission spectroscopy, J. Electron Spectros. Relat. Phenomena **114-116**, 729 (2001).

[83] M. Neupane, N. Alidoust, I. Belopolski, G. Bian, S.-Y. Xu, D.-J. Kim, P. P. Shibayev, D. S. Sanchez, H. Zheng, T.-R. Chang, H.-T. Jeng, P. S. Riseborough, H. Lin, A. Bansil, T. Durakiewicz, Z. Fisk, and M. Z. Hasan, Fermi surface topology and hot spot distribution in the Kondo lattice system CeB_6, Phys. Rev. B **92**, 104420 (2015).

[84] J. K. Lang, Y. Baer, and P. A. Cox, Study of the 4f and valence band density of states in rare-earth metals. II. Experiment and results, J. Phys. F: Met. Phys. **11**, 121 (1981).

[85] J. F. Herbst, R. E. Watson, and J. W. Wilkins, $4f$ excitation energies in rare-earth metals: Relativistic calculations, Phys. Rev. B **13**, 1439 (1976).

[86] J. F. Herbst, R. E. Watson, and J. W. Wilkins, Relativistic calculations of $4f$ excitation energies in the rare-earth metals: Further results, Phys. Rev. B **17**, 3089 (1978).

[87] H. Shinaoka, J. Otsuki, M. Kawamura, N. Takemori, and K. Yoshimi, DCore: Integrated DMFT software for correlated electrons, SciPost Phys. **10**, 117 (2020).

[88] O. Parcollet, M. Ferrero, T. Ayral, H. Hafermann, I. Krivenko, L. Messio, and P. Seth, TRIQS: A toolbox for research on interacting quantum systems, Comput. Phys. Commun. **196**, 398 (2015).

[89] M. Aichhorn, L. Pourovskii, P. Seth, V. Vildosola, M. Zingl, O. E. Peil, X. Deng, J. Mravlje, G. J. Kraberger, C. Martins, M. Ferrero, and O. Parcollet, TRIQS/DFTTools: A TRIQS application for *ab initio* calculations of correlated materials, Comput. Phys. Commun. **204**, 200 (2016).

[90] A. E. Antipov, I. Krivenko, and S. Iskakov, aeantipov/pomerol: 1.2, 2017.

[91] S. Lebègue, A. Svane, M. I. Katsnelson, A. I. Lichtenstein, and O. Eriksson, Multiplet effects in the electronic structure of light rare-earth metals, Phys. Rev. B **74**, 045114 (2006).

[92] S. Lebègue, A. Svane, M. I. Katsnelson, A. I. Lichtenstein, and O. Eriksson, Multiplet effects in the electronic structure of heavy rare-earth metals, J. Phys.: Condens. Matter **18**, 6329 (2006).

[93] I. L. M. Locht, Y. O. Kvashnin, D. C. M. Rodrigues, M. Pereiro, A. Bergman, L. Bergqvist, A. I. Lichtenstein, M. I. Katsnelson, A. Delin, A. B. Klautau, B. Johansson, I. Di Marco, and O. Eriksson, Standard model of the rare earths analyzed from the Hubbard I approximation, Phys. Rev. B **94**, 085137 (2016).

[94] P. Delange, S. Biermann, T. Miyake, and L. Pourovskii, Crystal-field splittings in rare-earth-based hard magnets: An *ab initio* approach, Phys. Rev. B **96**, 155132 (2017).

[95] E. Gull, A. J. Millis, A. I. Lichtenstein, A. N. Rubtsov, M. Troyer, and P. Werner, Continuous-time Monte Carlo methods for quantum impurity models, Rev. Mod. Phys. **83**, 349 (2011).

[96] N. Sato, A. Sumiyama, S. Kunii, H. Nagano, and T. Kasuya, Interaction between Kondo states and the Hall effect of dense Kondo system $Ce_xLa_{1-x}B_6$, J. Phys. Soc. Jpn. **54**, 1923 (1985).

[97] W. Joss, J. M. van Ruitenbeek, G. W. Crabtree, J. L. Tholence, A. P. J. van Deursen, and Z. Fisk, Observation of the magnetic field dependence of the cyclotron mass in the Kondo lattice CeB_6, Phys. Rev. Lett. **59**, 1609 (1987).

[98] H. Harima, O. Sakai, T. Kasuya, and A. Yanase, New interpretation of the de Haas-van Alphen signals of LaB_6, Solid State Commun. **66**, 603 (1988).

[99] A. Koitzsch, N. Heming, M. Knupfer, B. Büchner, P. Y. Portnichenko, A. V. Dukhnenko, N. Y. Shitsevalova, V. B. Filipov, L. L. Lev, V. N. Strocov, J. Ollivier, and D. S. Inosov, Nesting-driven multipolar order in CeB_6 from photoemission tomography, Nat. Commun. **7**, 10876 (2016).

[100] M. Jarrell, Hubbard model in infinite dimensions: A quantum Monte Carlo study, Phys. Rev. Lett. **69**, 168 (1992).

[101] H. Kusunose, Description of multipole in f-electron systems, J. Phys. Soc. Jpn. **77**, 064710 (2008).

[102] A. Tagliavini, S. Hummel, N. Wentzell, S. Andergassen, A. Toschi, and G. Rohringer, Efficient Bethe-Salpeter equation treatment in dynamical mean-field theory, Phys. Rev. B **97**, 235140 (2018).

[103] H. Shinaoka, D. Geffroy, M. Wallerberger, J. Otsuki, K. Yoshimi, E. Gull, and J. Kuneš, Sparse sampling and tensor network representation of two-particle Green's functions, SciPost Phys. **8**, 012 (2020).

[104] M. Wallerberger, H. Shinaoka, and A. Kauch, Solving the Bethe-Salpeter equation with exponential convergence, Phys. Rev. Res. **3**, 033168 (2021).

[105] M. Kitatani, R. Arita, T. Schäfer, and K. Held, Strongly correlated superconductivity with long-range spatial fluctuations, J. Phys. Mater. **5**, 034005 (2022).